J Clust Sci (2017) 28:2979–2995
DOI 10.1007/s10876-017-1250-9

ORIGINAL PAPER

# Optimization of Influential Factors on the Photocatalytic Performance of $TiO_2$–Graphene Composite in Degradation of an Organic Dye by RSM Methodology

**Farnosh Tavakoli[1] · Alireza Badiei[1] · Fatemeh Yazdian[2] · Ghodsi Mohammadi Ziarani[3] · Jahanbakhsh Ghasemi[1]**

Received: 4 April 2017 / Published online: 25 July 2017


**Abstract** Photocatalytic behavior was investigated for $TiO_2$–graphene nanocomposite in the degradation of acid orange 7 (AO7) as a model pollutant under ultraviolet light in aqueous solution. XRD, SEM, TEM, DRS, FT-IR and EDX techniques were used for the characterization of the prepared nanocomposite. The effect of synthesis variables such as weight ratio of $TiO_2$ to graphene and operational key factors such as initial dye concentration, irradiation time, catalyst dosage and solution distance from UV lamp were studied in the photocatalytic degradation of AO7. This excellent catalytic ability is mainly attributed to the synergic effect of photocatalyst and adsorbent. The effect of operational variables was optimized for the photocatalytic degradation of AO7 as a pollutant model using the RSM technique. In this case, the amount of the determination coefficient ($R^2 = 0.97$) shows that 97% of the variability in the response could be described by the model. The maximum degradation efficiency (96%) was achieved at the optimum operational conditions: catalyst dosage of 0.5 g $L^{-1}$, the irradiation time of 50 min and distance the solution from UV lamp of 0.3 cm.

**Keywords** Graphene · $TiO_2$ · Photocatalyst · Ultraviolet light · Acid orange 7

✉ Alireza Badiei
abadiei@khayam.ut.ac.ir

[1] School of Chemistry, College of Science, University of Tehran, Tehran, Iran

[2] Department of Life Science Engineering, Faculty of New Science and Engineering, Tehran, Iran

[3] Department of Chemistry, Alzahra University, Vanak Square, P.O. Box 1993893973, Tehran, Iran

## Introduction

It is known, that the textile industry with its manufacturing process is characterized by the high consumption of resources like water, fuel and a large variety of chemicals [1]. Reactive dyes, including azo dyes, are widely used due to their higher performance. But many of them are environmentally extremely hazardous and are proven to be carcinogenic [2–4]. Hence, removal or degradation of organic pollutants is an important research subject. Considerable efforts have been devoted to developing a suitable purification method that can easily destroy these organic contaminants [5]. Nowadays it is well confirmed that advanced oxidation processes (AOPs) are the best-recommended technologies for the removal of different pollutants from water [6]. Heterogeneous photocatalysis oxidation, as the most popular AOP method, has been widely used for removal of water pollutants because of its advantages, especially capability of carrying out under ambient conditions [7–11].

Hereby a considerable attention was shown over the past years for $TiO_2$ as a photocatalyst with high activity, low cost, non-toxicity, high stability in aqueous solutions and a possible use of solar irradiation [12, 13]. $TiO_2$ with energy band gap about 3.2 eV, which implies an excitation at a wavelength <400 nm, is also able to reduce metallic ions besides the degradation of toxic organic compounds and its basic efficiency can be enhanced by coupling process [14, 15]. The quick recombination of photogenerated electron–hole pairs decreases the efficiency of $TiO_2$ as a photocatalyst in wastewater treatment process [16, 17].

However, practical applications of $TiO_2$ as an adsorbent or a photocatalyst in aqueous solutions are limited because of the recovery problems of fine $TiO_2$ particles [18]. Recently, attempts have been made to immobilize the $TiO_2$ particles on different supports, such as activated carbon [19], clay [20] and zeolites [21], to improve their separation from bulk water [22].

Graphene (GR) as a new carbon nanomaterial has many exceptional properties, such as high electron mobility, high transparency, flexible structure, and large theoretical specific surface area [23, 24]. It is worthy to mention that the nanoparticles are directly decorated on the graphene sheets and no molecular linkers are needed to bridge the nanoparticles and the graphene which may prevent additional trap states along the sheets. Therefore, many types of the second phase can be deposited on graphene sheets in the form of nanoparticles to impart new functionality to graphene aiming at catalytic, energy storage, photocatalytic, and optoelectronics applications [25]. Many different types of synthesis methods have been developed for preparing graphene–nanoparticles composites, includes three main strategies; pre-graphenization, post-graphenization and syn-graphenization [26, 27].

Considering its superior electron mobility and high specific surface area, graphene can be expected to improve the photocatalytic performance of semiconductor photocatalysts such as $TiO_2$, where graphene can act as an efficient electron acceptor to enhance the photoinduced charge transfer and to inhibit the recombination of the photogenerated electron–holes [28]. Thus, the combination of $TiO_2$

and graphene is promising to improve the photocatalytic performance of $TiO_2$. Most recently, Lightcap et al. [29] demonstrated that $TiO_2$–graphene composite shows an enhancement of photocatalytic activity for the degradation of methylene blue. Zhang et al. [30] pointed out that the $TiO_2$–graphene composite was a highly efficient photocatalyst for the degradation of gas-phase benzene. Zhang et al. [31] reported that a $TiO_2$–graphene composite prepared by growing $TiO_2$ nanocrystals on graphene oxide (GO) through hydrolysis of $Ti(BuO)_4$ has improved the photocatalytic activity of $TiO_2$ for the degradation of rhodamine B.

We employed response surface methodology (RSM) for statistically optimizing the operational and synthesis variables of $TiO_2$–AgI by using a minimum number of experiments. The RSM is a mathematical and statistical technique that is widely employed in optimizing and modeling process. RSM technique is capable of analyzing the interactions of possible influencing factors and determining the optimum region of the factors level just by using a minimum number of designed experiments.

In the present study, $TiO_2$–graphene composite was prepared via a combination of the ultrasonic and hydrothermal method. The photocatalytic performance of this composite was investigated for photodegradation of acid orange 7 (AO7) as a pollutant model. The effect of synthesis and operational variables, such as $TiO_2$ content, irradiation time, catalyst dosage and solution distance from UV lamp were studied in the photocatalytic degradation of AO7. On the other hands, the effect of operational variables were optimized for the photocatalytic degradation of AO7 as a pollutant model using the RSM technique. In this case, the amount of the determination coefficient ($R^2 = 0.97$) shows that 97% of the variability in the response could be described by the model. XRD, SEM, TEM, DRS, FT-IR and EDX techniques were used for the characterization of the prepared nanocomposite.

## Experimental

### Materials

All the reagents for the synthesis of $TiO_2$–graphene such as potassium iodide, graphite, $HNO_3$, $H_2SO_4$, $KMnO_4$, $H_2O_2$ and titanium dioxide were commercially available from Merck and employed without further purification.

The synthesis was carried out at atmospheric pressure and ambient temperature with an ultrasonic irradiation provided by a probe sonicator (Qsonica Q700, Newtown, CT, US). FT-IR spectra was recorded a 400–4000 $cm^{-1}$ region on Rayleigh WQF-510a. Powder X-ray diffraction (XRD) patterns were collected from a diffractometer of Philips Company with X'pertpro monochromatized Cu Kα radiation ($\lambda = 1.54$ Å). Microscopic morphology of products was visualized by SEM (MIRA3 TESCAN). TEM images were obtained on a CM30 transmission electron microscope with an accelerating voltage of 300 kV. The energy dispersive spectrometry (EDS) analysis was studied by XL30, Philips microscope. DRS of samples was obtained using AvaSpec 2048 TEC spectrometer for determination of the optical band gap ($E_g$) of pure $TiO_2$, pure AgI, $TiO_2$/AgI coupled nanoparticles

and the ternary composite of $TiO_2$–AgI–graphene. For determination of the $E_g$ Eq. (1) was used:

$$\alpha(h\upsilon) = B(h\upsilon - E_g)^{1/2} \quad (1)$$

where $\alpha$ is optical absorption coefficient, B is a constant dependent on the transition probability, $h$ is the Plank's constant and $\upsilon$ is the frequency of the radiation. The $E_g$ values were calculated by plotting $(\alpha h\upsilon)^2$ versus $h\upsilon$, followed by extrapolation of the linear part of the spectra to the energy axis.

### Preparation of Graphene Oxide

In this method, the improved Hummer method was applied to oxidize graphite for the synthesis of graphene oxide (GO) [32] from $H_2SO_4$, $HNO_3$, $KMnO_4$, $H_2O_2$ and distilled water.

### Preparation of $TiO_2$–Graphene Nanocomposite

A typical procedure for the synthesis of $TiO_2$–graphene nanocomposite is as follows: 0.2 g graphite oxide was dispersed in 10 mL water for 15 min under ultrasound irradiation. Then a solution containing 0.02 g $TiO_2$ in 10 mL of water was added dropwise into above mixture. After hydrothermal reaction at 80 °C for 5 h, graphene oxide was reduced to graphene nanosheets and $TiO_2$ nanoparticles were fixed on its surface to generate a $TiO_2$–graphene composite. Finally, the temperature of the mixture was brought down to room temperature and the mixture was filtered. The solid obtained was collected and washed with distilled water. After drying at 60 °C for 8 h, the $TiO_2$–graphene composite was obtained. In order to investigate the effect of different weight ratios of $TiO_2$ in as synthesized composite, seven different weight ratios of $TiO_2$ to the graphene were prepared.

### Photocatalytic Degradation Experiment

The photocatalytic degradation processes were carried out at room temperature in a batch quartz reactor. Artificial irradiation was provided by an 8 W (UV-C) mercury lamp (Philips, Holland) emitting around 254 nm, positioned in the top of the batch quartz reactor. In each run, 40 mg of catalyst was dispersed in 100 mL water, then desired concentration of AO7 (20 mg $L^{-1}$) and photocatalyst (400 mg $L^{-1}$) were transferred into the batch quartz reactor and was stirred for 30 min to reach the adsorption equilibration in the dark before irradiation. The photocatalytic reaction was initiated by turning on the light source. At given irradiation time intervals, the samples (5 mL) were retrieved, centrifuged (sigma 2-16p) and then the AO7 concentration was analyzed by UV–vis spectrophotometer (Rayleigh UV-1600) at $\lambda_{max} = 485$ nm. All experiments were performed in initial pH of dye solution (pH 6.1). The degradation efficiency is calculated by Eq. (2):

$$\text{Degradation efficiency (DE}(\%)) = (C_0 - C_t/C_0) \times 100 \quad (2)$$

where C0 and C are the AO7 concentration (mg $L^{-1}$) at the time 0 and t.

### Experimental Design

Optimization of degradation percentage versus operational variables was considered via statistical analysis. Catalyst dosage (mg/L) (A) and distance of solution from a lamp (cm) (B) were selected as effective factors. Analysis was used in order to study the relationship between these variables and the optimum levels of them. For this purpose, ten experimental runs were required as per five-level central composite design (CCD). The results and predicted responses are offered (Table 1). Data from CCD were exposed to a regression analysis to describe the behavior of the system using the least squares regression procedure to obtain the factor estimators of the mathematical typical.

## Results and Discussion

Based on our previous papers that were published in 2014 and 2015 graphene oxide was synthesized and characterized by using SEM, XRD and FT-IR [23, 24]. According to XRD pattern, FT-IR and SEM images of graphite and graphene oxide (GO), the as prepared GO was properly synthesized.

### Characterization and Photocatalytic Performance of $TiO_2$–G

Figure 1a–c shows the XRD patterns of $TiO_2$–G, $TiO_2$ and graphene oxide. The diffractogram of graphene oxide exhibited the typical reflections at $2\theta = 26.48°$ and 43.17° corresponding to the (002) and (100) reflections (JCPDS 01-0646) (Fig. 1c). According to Fig. 1b For the $TiO_2$ compound, the XRD diffraction reflections at $2\theta$ of 25.8°, 38°, 39.5°, 48°, 55°, 62.6°, 69.7° and 75.7° can be indexed to the characteristic reflections of the (101), (004), (112), (200), (211), (213), (220) and

**Table 1** The experimental design according to RSM for optimization of key factors

| A | B |
|---|---|
| −1 | −1 |
| 1 | −1 |
| −1 | 1 |
| 1 | 1 |
| −1.41 | 0 |
| 1.41 | 0 |
| 0 | −1.41 |
| 0 | 1.41 |
| 0 | 0 |
| 0 | 0 |

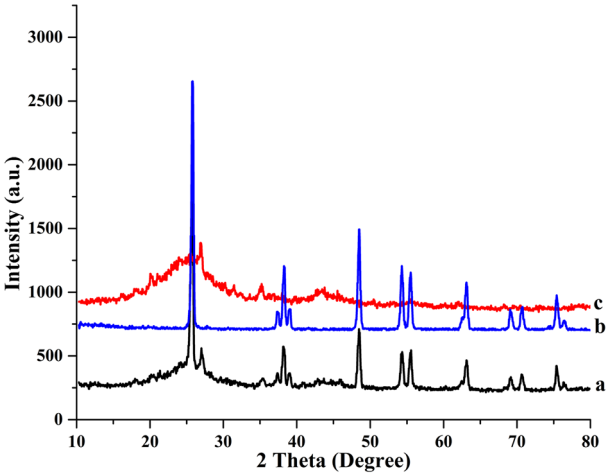


**Fig. 1** XRD patterns of: *a* $TiO_2$–G; *b* $TiO_2$; *c* GO

(215) plane reflections of anatase crystal structure $TiO_2$. However, for the $TiO_2$–graphene composite, only the reflections from $TiO_2$ were detected. The (002) and (100) reflection of graphene overlapped the anatase (200) and (113) reflection of $TiO_2$. However, for the $TiO_2$–graphene composite, only the reflections from $TiO_2$ were detected. The (002) reflection of graphene oxide overlapped the anatase (200) reflection of $TiO_2$. Therefore, the intensity of the reflection at $2\theta = 25.8°$ from the $TiO_2$–graphene composite was stronger than that from the $TiO_2$ compound.

Figure 2a–c show the SEM images of graphene, $TiO_2$, and $TiO_2$–G. As shown in Fig. 2a, graphene nanosheets are individually exfoliated. According to Fig. 2b spherical morphology of $TiO_2$ is shown. Figure 2c shows the SEM images of the $TiO_2$–graphene composite. According to this image, spherical $TiO_2$ compounds were observed on the graphene sheets and particles were coated on the surface of the graphene. SEM images of graphene (Fig. 2a) and $TiO_2$–graphene composite (Fig. 2c) show the best distribution of $TiO_2$ particles on the graphene sheets.

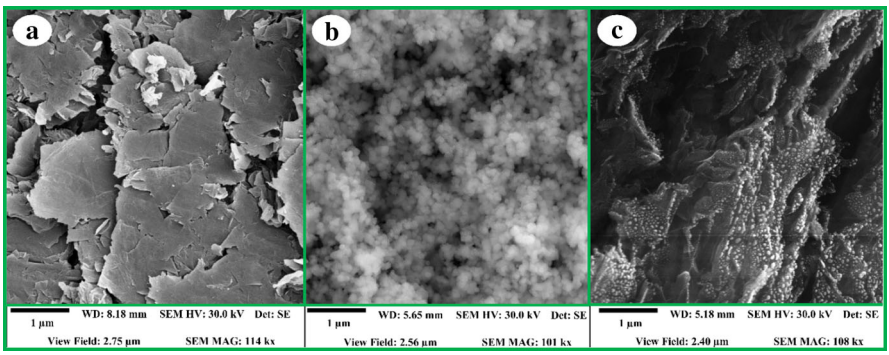


**Fig. 2** SEM images of: **a** graphene; **b** $TiO_2$; **c** $TiO_2$–G

TEM images of graphene and $TiO_2$–G composite are shown in Fig. 3a, b respectively. According to TEM images, $TiO_2$ particles are mounted on the graphene sheet surfaces and some particles intercalate between the graphene interlayer.

To get information on the elements, the $TiO_2$–G composite was examined by EDX analysis. Figure 4 show the EDX analysis of the $TiO_2$–G composite. In the EDX spectrum of $TiO_2$–G composite, the main elements such as Ti, O and C were presented. According to EDX analysis, results confirmed the existence of $TiO_2$ nanoparticles on the surface of graphene. $TiO_2$ being present on the graphene surface emerged to trap the migrated electron ($e^-$), leaving the holes ($h^+$) free to react with water molecules to form hydroxyl radicals, which in turn could have degraded pollutant molecules and prevented the rapid recombination with electrons.

Since the synthesis procedure of $TiO_2$–G was post-graphenization, so we used graphene oxide for synthesized the $TiO_2$–G composite. Because graphene oxide is a hydrophilic compound due to presence of oxygen functional group on its surface,

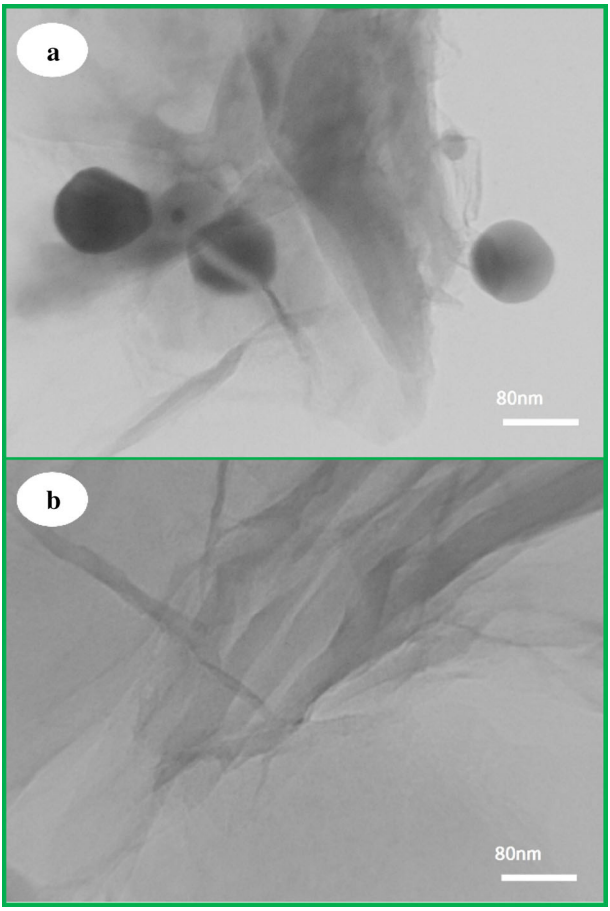


**Fig. 3** TEM images of: **a** $TiO_2$–G; **b** graphene oxide

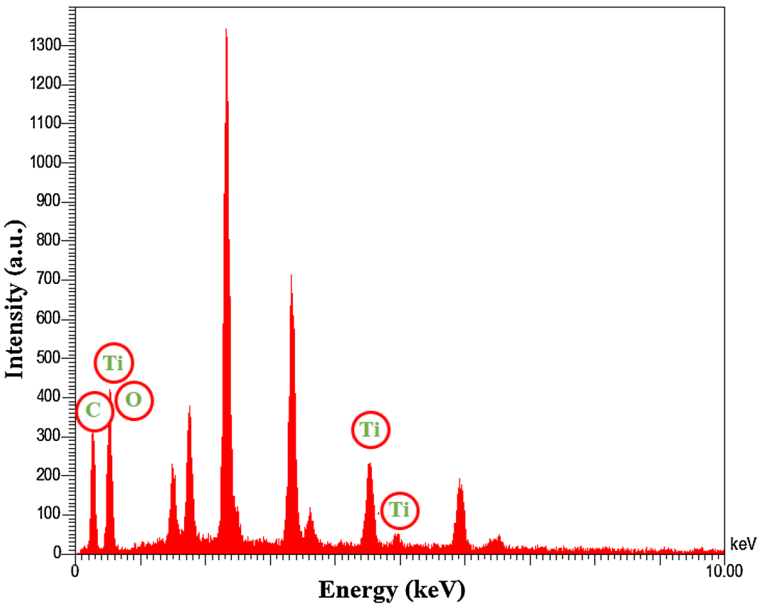


**Fig. 4** EDX spectrums of $TiO_2$–G

so, this combination is well dispersible in water. On the other hands, $TiO_2$ is a hydrophilic compound that can connect to graphene oxide surface via hydrogen-bond to oxygen groups. Since there is no thermal stage in the preparation method of $TiO_2$–G nanocomposite, so, after being on the graphene surface, not change is shown in the $TiO_2$ phase. We suspected that, since there has been no change in the $TiO_2$ phase, so $TiO_2$'s chemical surrounding have not any change after combining with rGO. Finally, as shown in SEM and TEM images, spherical $TiO_2$ nanoparticles placed on the surface of graphene oxide.

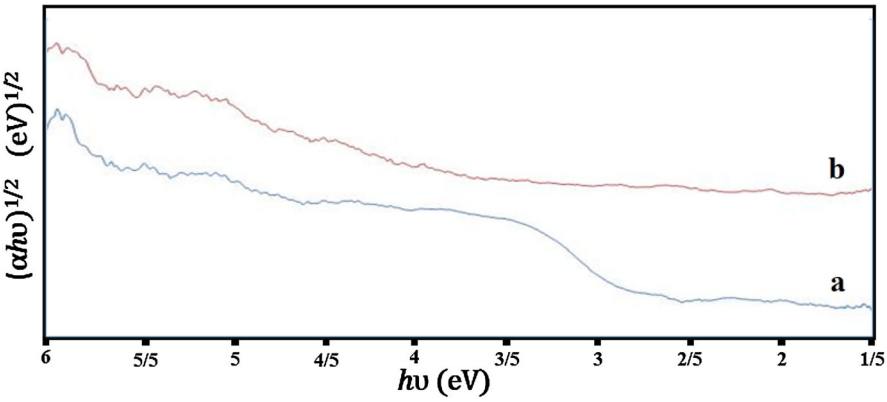


**Fig. 5** Diffuse reflectance absorption spectra of: *a* $TiO_2$; *b* $TiO_2$–G

UV–visible diffused reflectance spectra of $TiO_2$ and $TiO_2$–G were shown in Fig. 5. Compared with absorption edge of $TiO_2$ which was detected at around 399 nm, a red shift to the higher wavelength at 425 nm in the absorption edge of $TiO_2$–G sample could be observed. It means that the $TiO_2$–G catalyst underwent a red shift of about 26 nm. This result indicated that the narrowing of the band gap of $TiO_2$ occurred with the graphene introduction and on the other hand, this narrowing should be attributed to the Ti–O–C bonds. In the case of $TiO_2$–G nanocomposite, a heterojunction forms at the interface, where there is a space-charge separation region. Electrons have a tendency to flow from the higher to lower Fermi level to adjust the Fermi energy levels. The calculated work function of graphene is 4.42 eV and the conduction band position of anatase $TiO_2$ is about −4.21 eV with a band gap of about 3.2 eV, graphene can accept the photoexcited electrons from $TiO_2$. So, the photoinduced electron–hole pairs are effectively separated and the probability of electron–hole recombination is reduced.

The valence band (VB) and conduction band (CB) potentials of semiconductors are two important factors for the effective separation of photogenerated electron–hole pairs to generate OH radicals and superoxide anions. The VB and CB potential edges were calculated using the following empirical formula [32, 33].

$$E_{VB} = X - E^e + 0.5\left(E_g\right)$$

$$E_{CB} = E_{VB} - E_g$$

where $E_{VB}$ and $E_{CB}$ are the valence and conduction band edge potentials of a semiconductor, respectively, X is the electronegativity value of the semiconductor, which is the geometric mean of the electronegativities of constituent atoms, $E^e$ is the energy of free electrons on the hydrogen scale ($\sim$4.5 eV), $E_g$ is the band gap energy of the semiconductor.

The photocatalytic performance of the prepared catalysts was evaluated using aqueous AO7 dye as a model compound under UV light irradiation. It is well known that the adsorption of dye molecules on catalyst surface is one of the key factors for the degradation of organic pollutants [31]. Especially carbon based materials have shown excellent adsorption capacity. Compared to $TiO_2$, graphene loaded composite shows higher adsorption of dye molecules. This increase in dye adsorption on catalytic surfaces plays a significant role for achieving higher photocatalytic activity.

Figure 6 displays UV–vis absorption spectra of the $TiO_2$–G composite, pure $TiO_2$ and rGO. The enhanced absorption of the $TiO_2$–G composites compared to $TiO_2$ can be attributed to the presence of graphene. However, the obvious redshift of absorption edge in comparison with the pure $TiO_2$ may suggest a rearrangement of the energy level of $TiO_2$. This variation of the absorption property of $TiO_2$ is expected to enhance the utilizing efficiency of solar energy in photocatalysis. The absorption peak at 235 nm in the UV–vis spectrum of rGO correspond to π–π* transition of the remaining $sp^2$ C=C bonds.

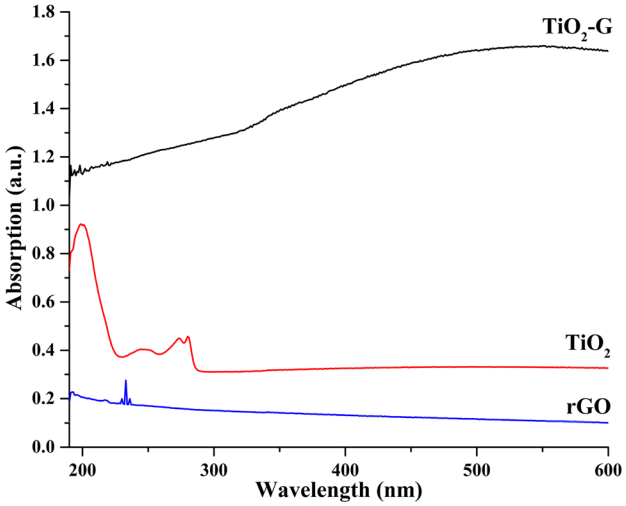


**Fig. 6** UV–vis absorption spectra of the $TiO_2$–G composite, pure $TiO_2$ and rGO

## Optimization of Synthesis Variables

### *Effect of $TiO_2$ Content*

As shown in Fig. 7, when experiments were carried out without catalyst, no degradation of AO7 was observed indicating that AO7 was not degraded when

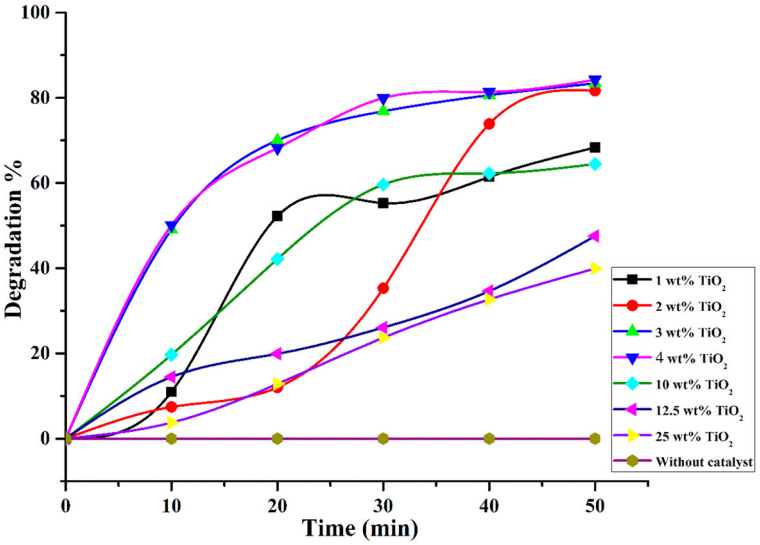


**Fig. 7** Degradation curve of AO7 aqueous dye with: UV light without photocatalyst; different weight ratio of $TiO_2$ to graphene

exposed to UV light. This observation clearly attributes that degradation of AO7 depends on the role of the photocatalyst. In order to evaluate the effect of $TiO_2$ loading, the different weight ratio of $TiO_2$ (1, 2, 3, 4, 10, 12.5 and 25wt%) were loaded to graphene and their photocatalytic performance was also tested under identical experimental conditions. The composite with 4wt% $TiO_2$ showed enhanced photocatalytic degradation compared to that of pure graphene and bare $TiO_2$ nanoparticle, whereas 12.5 and 25wt% $TiO_2$ loaded graphene photocatalyst decreased the photocatalytic activity. As shown in Fig. 7, with increasing the weight ratio of $TiO_2$ to graphene, the photodegradation performance of composite for AO7 was decreased, these results arise from increased the recombination rate instead of Impressive carrier separation, decreased the specific surface area and adsorptivity of graphene for adsorb dye molecules, thereby affecting the photodegradation and also cause disruption in the delivery of light to the photocatalyst. It can be seen in Fig. 7 that graphene with 4wt% $TiO_2$ exhibits 84.26% AO7 degradation within 50 min but only 61.14 and 36.03% of degradation occurred by bare $TiO_2$ and graphene, respectively. This enhancement in degradation was achieved due to the synergic effect in the $TiO_2$–graphene composite. Overlap the conduction bands of $TiO_2$ and graphene resulting in an amazing separation of charge carrier between graphene and the $TiO_2$ interface.

Increasing adsorption and specific surface area those are related to loading graphene, the formation of $\prod$–$\prod$ conjugations between dye molecules and aromatic rings of graphene and finally, the formation of ionic interactions between dye molecules and oxygen-containing functional groups of graphene are important factors that play a crucial role in the degradation of dyes. Here, graphene prevented the rapid recombination of electrons and holes because it plays the roles of adsorbent and electron acceptor.

As shown in Fig. 8, when only AO7 dye was exposed to UV light, no degradation of AO7 was observed. According to this observation degradation of AO7 is only due to the presence of photocatalyst. As shown in Fig. 8, photocatalytic performance of $TiO_2$–G (84%) composite for photodegradation of AO7 enhanced compared to pure $TiO_2$ (61%) and rGO (36%).

## Optimization of Operational Variables with RSM Method

The aim of conducting experimental design is to optimize degradation amount. The experimental design protocol and the corresponding results are obtained (Table 1). The experimental results of the CCD were fitted with a second order equation. A number of regression coefficients were considered and the fitted equation (in terms of coded values) for prediction of $k_La$ (Y) was as follows ($R^2 = 0.97$)

$$R1 = +0.78 + 0.073 * A - 0.081 * B - 0.14 * A^2 + 0.051 * B^2$$

where A and B are catalyst dosage (mg/L) and distance of solution from lamp (cm), respectively. The coefficients of the regression model (Eq. 1) that seems as one constant, two linear and two quadratics are listed in Table 1 The importation of each coefficient, determined by $p$ values, is also given in this table.

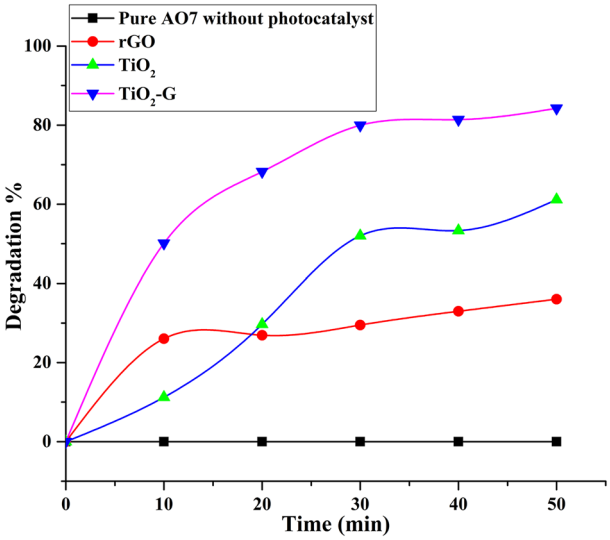


**Fig. 8** Photoreaction of AO7 solution under UV lamp and photocatalytic performance of rGO, $TiO_2$ and $TiO_2$–G

The first order of catalyst dosage and distance of solution from the lamp are taken to be important, also. Consequently, they can act as effective parameters since differences values of them will change degradation amount to a considerable extent. It is essential to test the important and the adequacy of the model through analysis of the variance. The *F* value or Fisher variance ratio is a statistically valid measure of how well the factors describe the variation in the data about its mean. The greater the *F* value, the more certain it is that the parameters explain adequately the variation in the data around its mean, and the estimated factor effects are real. The analysis of variance of the regression model demonstrates that the model is important, as is evident from the Fisher's *F* test. The goodness of fit with the quadratic model was established by the determination coefficient ($R^2$). In this case, the amount of the determination coefficient ($R^2 = 0.97$) shows that 97% of the variability in the response could be described by the model. The optimum values of the variables; obtained by the differentiation of the quadratic model, for achieving maximum photo-degradation of organic dye. The predicted optimal degradation value corresponding to these values is about 92%. To confirm the model precision for predicting the maximum value of photo-degradation, additional experiments in triplicates using the optimized key factors were performed. As shown in Table 1, the experimentally determined photo-degradation amount at optimum conditions (A: 0.27 and B: 1) was 92%, which agreed relatively well with model prediction. The 2D contour plots are the graphical representation of the regression equation and are plotted to recognize the interaction of the variables. The non-elliptical contour plots show that the interaction is not important for the development of optimal photo-degradation. The whole relationships between factors and response can be better understood by examining the planned series of contour plots (Fig. 9)

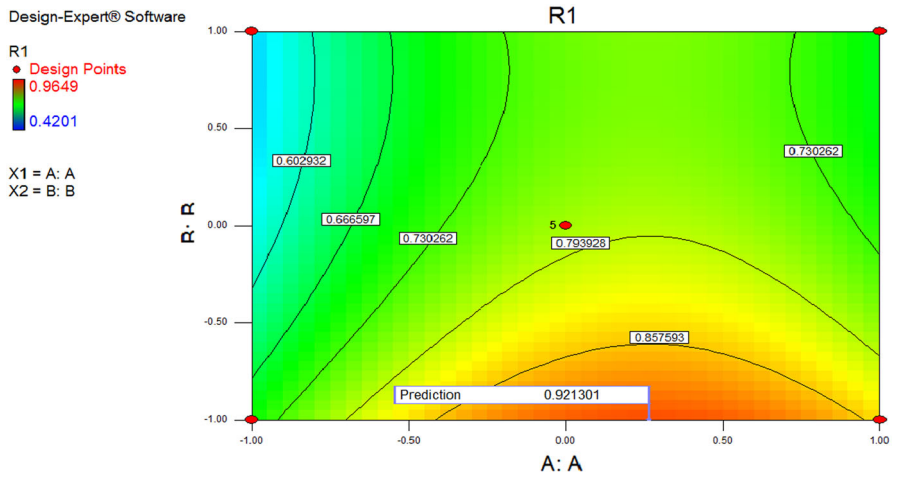


**Fig. 9** Contour plot for photo-degradation (%)

generated from the predicted models (Eq. 1). Figure 9 represents contour plot between the responses i.e. photo-degradation value (%) and the combined effect of initial dye and catalyst dosage on the photo-degradation (%). The figure shows that the amount of photo-degradation (%) enhanced in the middle amount of catalyst dosage and also increased after decreasing from maximum amount (Table 2).

*Effect of Initial Dye Concentration and Irradiation Time on Degradation Efficiency*

Figure 10 shows the initial dye concentration and irradiation time effect on the photodegradation of AO7, while rest of the parameters kept constant (10 cm distance of the solution from UV lamp and catalyst dosage of 0.4 g $L^{-1}$). As shown in the Fig. 10 the increase in the initial concentration of AO7 from 10 to 30 mg $L^{-1}$, decreases the photodegradation efficiency from 94 to 65%. When the initial concentration of the AO7 increases, the photons scattered before they can reach the $TiO_2$–G composite surface [34, 35]. Therefore, the absorption of photons by the $TiO_2$–G catalysts decreased and subsequently, the photodegradation efficiency decreased. On the other hand, with increasing of AO7 concentration more organic substances (AO7 and intermediates) are adsorbed on the surface of

**Table 2** ANOVA of the model for photo-degradation amount

| Source | Sum of squares | Mean squares | *F* value | *p* value |
|---|---|---|---|---|
| A–A | 0.042 | 0.042 | 45.21 | 0.0003 |
| B–B | 0.052 | 0.052 | 55.98 | 0.0001 |
| AB | 1.11E−003 | 1.11E−003 | 1.20 | 0.3101 |
| $A^2$ | 0.13 | 0.13 | 137.14 | 0.0001 |
| $B^2$ | 0.018 | 0.018 | 19.32 | 0.0032 |

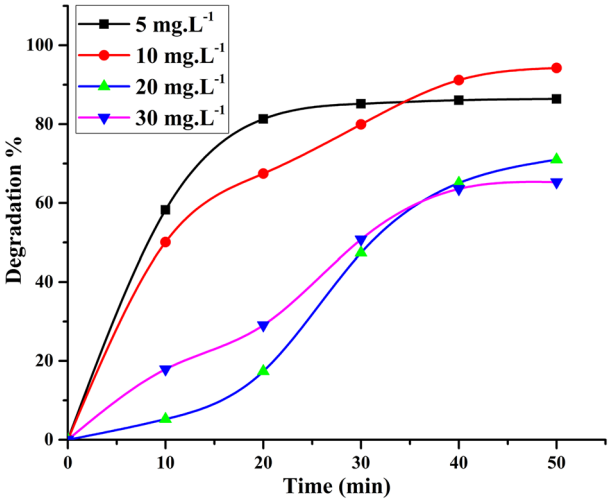


**Fig. 10** Degradation curve of AO7 aqueous dye with different initial dyes: 5 mg $L^{-1}$; 10 mg $L^{-1}$; 20 mg $L^{-1}$; 30 mg $L^{-1}$

$TiO_2$–G catalysts, therefore the generation of active species such as hydroxyl radicals will be reduced [36].

According to results, irradiation time has the impressive effect on photodegradation of AO7. For all initial dye concentration highest photocatalytic removal efficiency was obtained after an irradiation time of 50 min as shown in Figs. 8, 9 and 10 the photocatalytic removal efficiency of AO7 and UV irradiation time have a direct relationship.

*Effect of Catalyst Dosage and Irradiation Time on Degradation Efficiency*

As can be understood from RSM results the increase in the $TiO_2$–G dosage from 0.2 to 0.5 g $L^{-1}$ improves the removal efficiency of AO7 from 70 to 96%. These observations are the result of increasing catalytic and adsorption sites on the surface of $TiO_2$–G which are affected the photocatalytic activity. However, further increasing of the $TiO_2$–G dosage have no effect on removal efficiency of AO7. Increasing of the catalyst dosage from 0.5 to 0.8 g $L^{-1}$ can slightly decrease the photodegradation of AO7 from 96 to 64%. Why so, at high $TiO_2$–G catalyst loading scattering effect and turbidity of aqueous solution increases which causes a decrease in UV light penetration to the solution [37]. So, the absorption of photons by the catalyst surface decreased and subsequently, the photocatalytic removal efficiency of AO7 decreased.

*Effect of Solution Distance from UV Lamp and Irradiation Time on Degradation Efficiency*

Figure 9 shows the effect of the solution distance from UV lamp on the photocatalytic activity of $TiO_2$–G nanocomposite, while two other variables kept

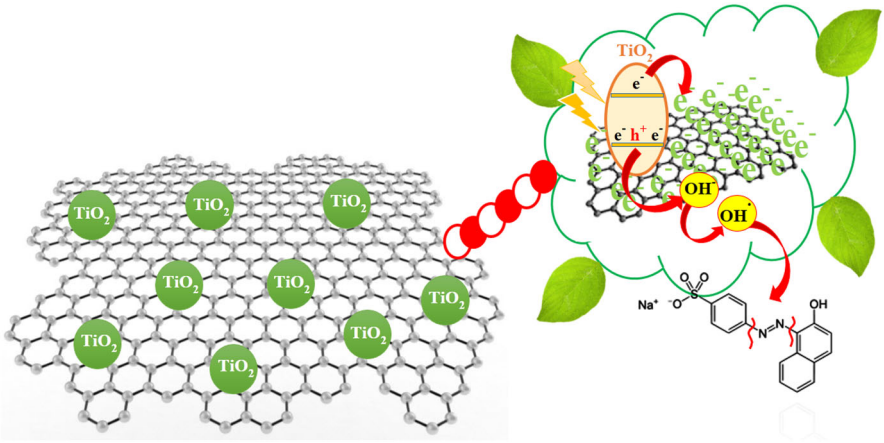


**Fig. 11** Photocatalytic mechanism of AO7 photodegradation with $TiO_2$–G composite

at their respective zero level (catalyst dosage of 0.5 g $L^{-1}$ and the irradiation time of 50 min). According to results, the removal efficiency increased from 51 to 96% with the decrease of the distance between the solution and UV lamp from 10 to 2 cm. Since, in lower distance to the lamp, the UV light irradiation produces the photons needed for the transferring of electron from the valence band to the conduction band of the $TiO_2$–G catalyst. Therefore, when the UV light intensity is low, faster recombination of electrons and holes occurs and decreases the formation of hydroxyl radicals and because hydroxyl radicals have a direct relation with photocatalytic removal efficiency, subsequently the photodegradation of AO7 decreased [38]. But, when more UV radiations reach to the surface of $TiO_2$–G catalyst, more hydroxyl radicals are produced and the photodegradation rate of AO7 dye increased [39]. The highest photocatalytic removal efficiency has direct and indirect relationship with irradiation time and distance between UV lamp and the solution, respectively.

## Photocatalytic Mechanism

$TiO_2$–G photocatalyst can absorb UV light to produce photogenerated electron–hole pairs due to the appearance of impurity energy levels. Normally in pure $TiO_2$ photocatalyst, the photogenerated electrons will be quickly recombined and only a small fraction of photogenerated electrons and holes may participate in the photocatalytic reaction, thus lead to the low photocatalytic activity, whereas the photogenerated electrons can be trapped by carbon atoms on the surface and $O_2$ molecules adsorbed on the surface of $TiO_2$–G to form superoxide anion radicals. This could effectively restrain the recombination of photogenerated electrons and holes. Subsequently, the generated $O_2$ on the surface of $TiO_2$–G photocatalysts will further react with electrons and $h^+$ in succession to form active OH radicals. The produced OH radicals are the main oxidizing.

Species responsible for the subsequent degradation of pollutants as confirmed by the above active species trapping experiments shown in Fig. 11. Meanwhile, the photogenerated holes may directly oxidize organic dyes or react with $OH^-$ to form OH radicals, which is subsequently involved in the degradation reaction.

The possible proposed photocatalytic reaction pathway mechanism of AO7 degradation over $TiO_2$–G nanocomposite is illustrated in Fig. 11. When $TiO_2$–G was irradiated with UV light, electrons from the valence band (VB) of $TiO_2$ are excited to the conduction band (CB) of $TiO_2$ and so, leaving positively charged holes in the valence bond. Furthermore, interfacial carrier separations take place with the aid of graphene. Since the CB work function of $TiO_2$ matches with CB work function of graphene, electrons can be easily transferred from CB of $TiO_2$ to graphene [40].

As a result, the oxygen sites can readily accept the electrons and undergo reduction reaction to generate more $O_2^{-\cdot}$ radicals. Thus, the presence of graphene in photocatalysts can produce an excess amount of reactive $O_2^{-\cdot}$ radicals due to good electron acceptor and transporter behavior of graphene. Therefore, the ultrafast transportation of photogenerated electrons over graphene sheet can directly reduce $O_2$ to produce $O_2^{-\cdot}$ radicals which lead to enhanced AO7 degradation.

## Conclusion

$TiO_2$–G nanocomposite was synthesized by using ultrasound irradiation and then it was used for degradation of AO7 as a model pollutant. XRD, SEM, TEM, DRS, FT-IR and EDX techniques were used for the characterization of the prepared nanocomposite. Several operational and synthetic parameters were investigated in degradation of AO7 by $TiO_2$–G nanocomposite. The effect of synthesis variables such as weight ratio of $TiO_2$ to graphene and operational key factors such as initial dye concentration, irradiation time, catalyst dosage and solution distance from UV lamp were studied in the photocatalytic degradation of AO7. The optimum amount of all factors were obtained. According to our results, the maximum degradation efficiency (94%) was achieved at the optimum operational conditions: initial AO7 concentration of 10 mg $L^{-1}$, catalyst dosage of 0.4 g $L^{-1}$, the irradiation time of 50 min and distance the solution from UV lamp of 2.5 cm.

**Acknowledgements** Authors are grateful to Council of University of Tehran and Center for International Scientific Studies Collaboration for providing financial support to undertake this work.

## References

1. T. Robinson, G. McMullan, R. Marchant, and P. Nigam (2001). *Bioresour Technol* **77**, 247.
2. B. Y. Chen, M. M. Zhang, C. T. Chang, Y. Ding, K. L. Lin, C. S. Chiou, C. C. Hsueh, and H. Xu (2010). *Bioresour Technol* **101**, 4737.
3. I. Arslan Alaton and J. L. Ferry (2002). *Dyes Pigm* **54**, 25.
4. K. Golka, S. Kopps, and Z. W. Myslak (2004). *Toxicol. Lett* **151**, 203.
5. F. Saadati, N. Keramati, and M. Mehdipour Ghazi (2016). *Environmental Science and Technology* **46**, 757.

6. X. Li, F. Chen, C. Lian, S. Zheng, Q. Hu, S. Duo, W. Li, and C. Hu (2016). *Journal of Cluster Science* **27**, 1877.
7. A. R. Nezamzadeh-Ejhieh and A. Shirzadi (2014). *Chemosphere* **107**, 136.
8. L. Yue, Sh Wang, G. Shan, W. Wu, L. Qiang, and L. Zhu (2015). *Applied Catalysis B: Environmental* **176**, 11.
9. Z. Xian, R. Liu, H. Li, S. Zhang, Z. Yang, W. Zheng, and C. Chen (2016). *Journal of Cluster Science* **27**, 241.
10. Z. Yaping, J. Chengguang, P. Ran, M. A. Feng, and O. U. Guangnan (2014). *Journal of Central South University* **21**, 310.
11. A. Azarian (2015). *Journal of Cluster Science* **26**, 1607.
12. J. Zhang, G. F. Huang, D. Li, B. X. Zhou, S. Chang, A. Pan, and W. Q. Huang (2016). *Appl. Phys. A* **122**, 994.
13. X. Wang, Y. Sang, X. Yu, B. Liu, and H. Liu (2016). *Appl. Phys. A* **122**, 884.
14. A. Alinsafi, F. Evenou, E. M. Abdulkarim, M. N. Pons, O. Zahraa, A. Benhammou, A. Yaacoubi, and A. Nejmeddine (2007). *Dyes Pigm* **74**, 439.
15. D. Beydoun, R. Amal, G. Low, and S. McEvoy (1999). *J. Nanopart. Res* **1**, 4394.
16. T. Yoshida, N. Yaghi, R. Nakagou, A. Sugimura, and I. Umezu (2014). Appl. Phys. A, DOI: 10.1007/s00339-014-8378-3
17. J. Chen, Y. Qian, and X. Wei (2010). *J. Mater. Sci* **45**, 6018.
18. A. Abbasi, D. Ghanbari, M. Salavati-Niasari, and M. Hamadanin (2016). *Journal of Materials Science: Materials in Electronics*. doi:10.1007/s10854-016-4361-4.
19. J. W. Shi, J. T. Zheng, and X. J. Ji (2010). *Environmental Engineering Science* **27**, 923.
20. B. Paul, W. N. Martens, and R. L. Frost (2012). *Applied Clay Science* **57**, 49.
21. H. Wang, B. Yang, and W. J. Zhang (2010). *Advanced Materials Research* **129**, 733.
22. S. Liu, M. Lim, and R. Amal (2014). *Chemical Engineering Science* **105**, 46.
23. F. Tavakoli and M. Salavati Niasari (2014). *J. Ind & Eng chem* **20**, 3170.
24. M. Salavati Niasari and F. Tavakoli (2015). *J. Ind & Eng chem* **21**, 1208.
25. V. Singh, D. Joung, L. Zhai, S. Das, S. Khondaker, and S. Seal (2011). *Materials Science* **56**, 1178.
26. V. Singh, D. Joung, L. Zhai, S. Das, S. I. Khondaker, and S. Seal (2011). *Progress in Materials Science* **56**, 1178.
27. X. Zhang, X. Liu, W. Zheng, and J. Zhu (2012). *Carbohydrate Polymers* **88**, 26.
28. S. Escobedo, B. Serrano, A. Calzada, J. Moreira, and H. D. Lasa (2016). *Fuel* **181**, 438.
29. I. V. Lightcap, T. H. Kosel, and P. V. Kamat (2010). *Nano Lett* **10**, 577.
30. H. Zhang, X. J. Lv, Y. M. Li, Y. Wang, and J. H. Li (2010). *ACS Nano* **4**, 380.
31. Y. H. Zhang, Z. R. Tang, X. Z. Fu, and Y. J. Xu (2010). *ACS Nano* **4**, 7303.
32. X. Lin, J. Xing, W. Wang, Z. Shan, F. Xu, and F. Huang (2007). *J. Phys. Chem. C* **111**, 18288.
33. L. Chen, D. Jiang, T. He, Z. Wu, and M. Chen (2013). *Cryst. Eng. Commun* **15**, 7556.
34. M. A. Behnajady, N. Modirshahla, M. Shokri, H. Elham, and A. Zeininezhad (2008). *J. Environ. Sci. Health. Part A Toxic/Hazard. Subst. Environ. Eng* **43**, 460.
35. S. Chakrabarti and B. K. Dutta (2004). *J. Hazard. Mater* **112**, 269.
36. M. A. Behnajady, N. Modirshahla, N. Daneshvar, and M. Rabbani (2007). *Chem. Eng. J* **127**, 167.
37. L. A. Ghule, A. A. Patil, K. B. Sapnar, S. D. Dhole, and K. M. Garadkar (2011). *Toxicol. Environ. Chem* **93**, 623.
38. M.A. Behnajady, H. Eskandarloo, Res. Chem. Intermed. http://dx.doi.org/10.1007/s11164-013-1327-5.
39. B. Neppolian, H. C. Choi, S. Sakthivel, B. Arabindoo, and V. Murugesan (2002). *J. Hazard. Mater* **89**, 303.
40. S. D. Perera, R. G. Mariano, K. Vu, N. Nour, O. Seitz, Y. Chabal, and K. J. Balkus (2012). *ACS Catal* **2**, 949.